INTERNATIONAL JOURNAL OF REMOTE SENSING
2019, VOL. 40, NO. 13, 4876–4897
https://doi.org/10.1080/01431161.2019.1574995

Check for updates

Assessing uncertainty and demonstrating potential for estimating fire rate of spread at landscape scales based on time sequential airborne thermal infrared imaging

Douglas Stow [a], Philip Riggan[b], Gavin Schag[a], William Brewer[a], Robert Tissell[b], Janice Coen[c] and Emanuel Storey [a]

[a]Department of Geography, San Diego State University, San Diego, CA, USA; [b]Pacific Southwest Research Station, United States Forest Service, Riverside, CA, USA; [c]National Center for Atmospheric Research, Boulder, CO, USA

ABSTRACT
An important property of wildfire behaviour is rate of spread (ROS). The objectives of this study are to evaluate the uncertainty of landscape-scale ROS estimates derived from repetitive airborne thermal infrared (ATIR) georeferenced imagery and the utility of such estimates for understanding fire behaviour and controls on spread rates. Time-sequential ATIR image data were collected for the Cedar, Detwiler, and Rey Fires, which burned in California during summers of 2016 and 2017. We analyse error, uncertainty, and precision of ROS estimates associated with co-location accuracy, delineation of active fire front positions, and generation of fire spread vectors. The major sources of uncertainty influencing accuracy of ROS estimates are co-registration accuracy of sequential image pairs and procedures for delineating active fire front locations and spread vectors between them; none of these were found to be substantial. Median ROS estimates are 11 m min^{-1} for the Cedar Fire and 8 m min^{-1} for the Detwiler Fire, both of which burned through mixed shrub and tree areas of the Sierra Nevada foothills and were estimated for downslope spread events. Of the three study fires, the fastest spread rates (average spread of 25 m min^{-1} with maximum of 39 m min^{-1}) are estimated for the Rey Fire, which burned on variable directional slopes through chaparral shrubland vegetation.

ARTICLE HISTORY
Received 20 October 2018
Accepted 14 January 2019

1. Introduction

Understanding how fires burn in wildland areas is of great interest because of their effects on ecosystem functioning and their hazard potential for humans and structures. This is particularly the case for the State of California, USA, where extent of total burn area and burn area of wildfire events, and loss of life and property damage have increased markedly in the past several years (Barron and Gajanan 2018; Loomis 2018).

CONTACT Douglas Stow stow@mail.sdsu.edu Department of Geography, San Diego State University, San Diego, CA, USA

© 2019 Informa UK Limited, trading as Taylor & Francis Group

Thus, understanding and predicting the behaviour of wildland fires (wildfires for short) is of interest for scientific, resource management, and emergency management reasons.

An important property of wildfire behaviour is rate of spread (ROS) (also referred to as fire spread rate). Wildfire ROS varies spatially and temporally depending on three primary factors: (1) weather – wind speed and direction, relative humidity and surface temperature, (2) topography – slope angle and aspect, and (3) fuels – vegetation composition, structure, moisture content, and mass of dead and live material (Alexander and Cruz 2013; Beyers et al. 2007; Ji et al. 2014; Van Wagner 1977).

The primary impetus for our current research is to better understand relationships between weather, topographic, and fuel variables that control fire spread. These controls on fire behaviour have been evaluated (almost exclusively) based upon laboratory experiments or numerical model simulations (Cruz, Alexander, and Sullivan 2017), both of which may lead to limited insights unless the conditions and scales of actual wildland fire behaviours are captured empirically for validation. Measurements of both ROS and fire intensity from remote sensing data enable analyses of the interrelationship between and decoupling of these key fire behaviour variables. Similarly, fire ecologists are able to study fire effects on vegetation and ecosystems, since ROS and intensity relationships influence fire residence time, energy expenditure, burn severity, and presence of unburned patches. From a more practical, broader impacts perspective, if rapid and timely ROS estimates can be derived from remote sensing observations, resultant data can be transferred to incident commanders and emergency managers to inform decision-making for fire suppression and evacuations of humans and domesticated animals.

Observing fire spread and measuring ROS at landscape scales and over extensive wildland areas is challenging (Stow et al. 2014). Such observations and measurements are typically limited to controlled burn experiments over relatively small spatial scales or observations of fire perimeter expansion at large time scales based on airborne or satellite thermal infrared observations (Loboda and Csiszar 2007; Martinez-de Dios et al. 2011). Making finer-scale (in space and time) observations of wildfire spread requires frequent repeat passes from airborne thermal infrared (ATIR) imaging systems, typically limited to particular portions of the spreading fire perimeter such as the active fire front (Stow et al. 2014). Few studies other than Stow et al. (2014) have focused on measuring ROS for actual wildfires (i.e. not control burns) at relatively fine spatial (10^2–10^3 m) and temporal scales (10–10^2 min). Viedma et al. (2015) analysed landscape and fire behaviour influences on satellite-estimated fire severity within Spanish pine forests, including the influence of fire ROS and spread direction. These landscape-level fire propagation estimates were derived from aerial photography captured at repeat intervals that varied between 15 and 480 mins. No details were provided on how fire perimeter locations were delineated. ROS estimates varied between 0.4 and 214.2 m min^{-1}, with a mean spread of 6.7 m min^{-1}. Riggan et al. (2004) measured landscape-scale ROS of a prescribed fire in Brazilian cerrado with imagery from an extended dynamic range imaging spectrometer.

The objectives of this article are to evaluate the uncertainty of ROS estimates derived from repetitive ATIR georeferenced imagery and the utility of such estimates for understanding fire behaviour and controls on spread rates. We build on the Stow et al. (2014) study which was derived from archived ATIR imagery that had mostly been collected for purposes of mapping the entire fire perimeter. We process and analyse time sequential image sets for several wildfires that burned in different landscape types. While in most cases the ATIR image sets evaluated in this study were not captured and geoprocessed in an optimized manner, they enable estimation of ROS and descriptive analysis of landscape factors controlling ROS. We evaluate error, uncertainty and precision of ROS estimates associated with co-location accuracy, delineation of active fire front positions, and generation of fire spread vectors. Finally, we provide recommendations and consider theoretical elements of an idealized approach to estimating ROS and evaluating landscape covariates that likely control ROS.

2. Study fires and data

This study is based on ATIR image data collected for three wildfires in California that occurred during the summers of 2016 and 2017, namely the Cedar, Detwiler, and Rey Fires, as shown in Figure 1. (Note that the Cedar Fire of 2016 should not be confused with the more extensive Cedar Fire which burned in southern California in 2003.) These fires burned in very different weather conditions, terrain characteristics, and fuel types. All were imaged by the same commercial aerial survey company with a FireMapper 2.0 ATIR sensor system. The FireMapper 2.0 is a non-cryogenic sensor with a 320 × 240 frame array (Riggan and Hoffman 2003).

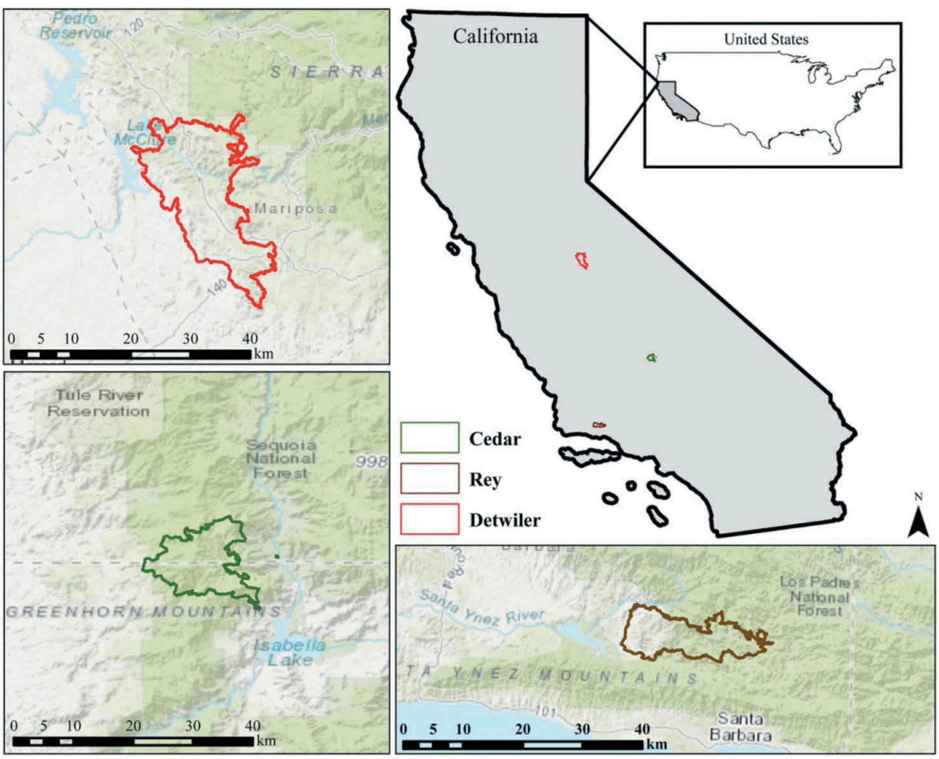

Figure 1. Three study wildfires in southern California. Shown on this map of California are the burn extents of the Cedar, Detwiler and Rey fires.

The primary purpose of the imaging missions was to monitor the expansion of the entire fire perimeter, with a secondary objective of higher frequency imaging of the active fire front portion of the perimeter (the focus of this study). This means that the collection pattern for repeat-pass imagery was suboptimal but still useful. Only small portions of the total burn areas were covered with overlapping, time sequential ATIR image frames, and evaluated for this study.

The Cedar Fire burned in summer 2016 in the western foothills of the southern portion of the Sierra Nevada range. The fire was ignited by an unknown human source and primarily spread in a southwest direction and burned through both temperate coniferous and shrubland fuels. ATIR imagery was collected in August 2016, with the primary goal of mapping changes in the perimeter. A few short-interval repeat imaging passes were attempted, but no useable image sets for ROS measurement were captured. However, the backing (spread opposite of wind direction) portion of the fire was imaged sequentially over an 18.5-hr period on 19 August 2016, enabling us to measure ROS in fuel dominating spread conditions.

Also in summer 2016, the Rey Fire spread mostly through chaparral shrubland north of Santa Barbara, CA near Lake Cachuma. The fire was ignited by a fallen tree over a powerline at a picnic area on August 18 and was declared fully contained a month later, after burning 132 km^2. ATIR imagery was collected during the third day of the fire on 21 August, such that a single repeat-pass image collection occurred with a 7-min repeat interval.

The Detwiler Fire burned an area of 330 km^2 from 16 July through 24 August 2017 within the Sierra Nevada foothills just west of Yosemite National Park. ATIR images were collected 19–21 July for the eastern portion of the active fire zone. During this period the fire burned through irregular terrain and a mixture of chaparral shrubland and woodland fuels. Most experimentation in generating and testing fire front curves and fire spread vectors, as well as buffering for landscape covariates analyses, was conducted with the Detwiler Fire datasets that were the most reliable and robust. This seven-image sequence was captured on 20 July 2017 using a repetitive ‘racetrack’ flight pattern.

Other datasets providing information on landscape covariates were also utilized in the study. We obtained colour infrared orthoimagery (0.5 m ground sampling distance) produced by the United States National Agriculture Imagery Program (NAIP). From this high spatial resolution orthoimagery captured in summer 2016 (prior to the three study fires), we generated normalized difference vegetation (NDVI) images based on uncalibrated digital number values, and for the Detwiler Fire study area, a map of growth forms (e.g. herbs, shrubs or trees), dead/diseased trees, and barren cover. We tested unsupervised pixel-based and supervised object-based classification approaches and found the map from the object-based approach to be the most reliable for purposes of demonstrating potential utility for quantifying landscape covariates of ROS. We generated three-dimensional visualizations, and directional slope and slope aspect data from 10 m raster National Elevation Dataset (digital elevation model) data provided by the United States Geological Survey.

3. Methods

We designed a sequence of image processing and analysis steps and applied them to the repeat-pass ATIR image pairs to estimate wildfire ROS and to descriptively examine landscape controls on ROS (Mermoz and Kitzberger 2005). These include geoprocessing individual image frames, delineating active fire front positions, generating fire spread vectors and ROS estimates based on changing front positions, extracting topographic and fuels data in the vicinity of spread vectors, and evaluating relationships between ROS and topographic and fuels covariates. Other than geometric processing (described below), most image processing and analysis was supported by image processing tools within ArcGIS Pro software.

FireMapper 2.0 image frames were geometrically processed using aircraft position and attitude, as recorded by an Applanix inertial measurement unit, together with interior camera parameters and a digital elevation model (ASTER 1 arcsecond data). In this process, raw FireMapper 2.0 images, which are sequentially stored with camera metadata and comprise streams of 16-bit unsigned-short digital-number values, are extracted as single-band arrays using the FireMapper Tools software application (ver. 3.4.2.258, USDA Forest Service, 2009). These 320-column by 240-row images were imported to the ERDAS Imagine 2014 Photogrammetry software application (Leica 2006), stored in Imagine IMG file format and loaded into an Imagine Photogrammetry block along with exterior orientation parameters and interior parameters including lens focal length, coefficients for radial lens distortion, and pitch size of the camera's focal-plane array. Approximate coefficients of radial lens distortion were estimated using imagery obtained over St. George, UT. These coefficients were refined with the use of Jacobsen's simple model during aerial triangulation within Imagine. Images were projected in UTM with GRS 1980 spheroid and NAD83 datum and bi-linearly resampled to produce individual orthoimages. These images were visually inspected, using an Imagine viewer, with reference to a National Agricultural Imagery Program image (with nominally 1-metre resolution) and to the overlap between sequential FireMapper 2.0 images. Ground control points and image tie points were added prior to aerial triangulation to revise the exterior orientation parameters and obtain the desired error from aerial triangulation: total image unit-weight root mean square error (RMSE) of less than or equal to 0.5 pixels and control point root RMSE less than or equal to 1.0 pixel for both X and Y coordinates. A radiometric calibration, based on laboratory calibrations with a high-temperature blackbody standard (Electro Optical Industries, Inc., model LS1250-100 Blackbody with model 2503B Temperature Controller) was further applied to obtain estimates of radiance at the sensor and equivalent blackbody temperatures. Orthoimages were merged using ERDAS Imagine Mosaic Pro.

We evaluated the co-registration accuracy of image pairs by automatically generating prospective test points (i.e. features that could be identified on both bi-temporal pair images) and manually selecting a subset of high-confidence, well-distributed points. We were careful to select points from stable hot spot features associated with recently burned or burning areas, or features just beyond the active fire front in unburned portions of the image scene. Positions of test points were extracted to the pixel-level for both images.

Georeferenced FireMapper 2.0 image pairs were simultaneously displayed and used to delineate active fire front positions and generate fire spread vectors between such positions. We developed and tested four image enhancement and delineation approaches to mapping active fire fronts: (1) brightness contrast stretch with manual delineation, (2) brightness contrast stretch with manual delineation followed by cartographic smoothing, (3) Laplacian (high pass) convolution filtering with manual delineation, and (4) brightness contouring with manual selection of contours that represented the apparent fire front position. We evaluated relative differences in positions of fire fronts delineated by the four approaches by measuring distances of the nearest point of each pair of delineated curves from regularly spaced (distance equivalent to five pixels) sample points. We also estimated the ROS between each type of delineated front using the normal vector from points on the time = *n* (earliest captured image of each sequential pair) curve approach described below.

The first step in creating fire spread vectors was to automatically generate evenly spaced points along the time = *n* fire front curve, from an initial staring point near one end of a delineated fire front curve. We experimented with different spacing distances, guided by theoretical considerations pertaining to oversampling, the width of buffers around spread vectors used for covariates analyses and desire to generate an adequate sample size, and empirically by evaluating frequency distributions of ROS estimates. (See Results and Discussion sections for details.) The direction of the local normal vector at each sample point was automatically determined using the Perpendicular function (Editing toolbar) in ArcGIS software. Vectors were formed by manually extending the line features to the point at which they intersected the time = *n* + 1 fire front curve. This was done for two different regular point spacings (referred to as Normal to curve – closer spacing and Normal to curve – wider spacing in Table 4). Vector directions were manually adjusted from the local normal direction in cases where vectors converged and intersected (e.g. associated with concave features on the time = *n* curve). We also used highly smoothed versions of the front curves to determine normal vector directions, with vectors emanating from each time = *n* curve (referred to as Normal to trend in Table 4). Finally, we tested a manual approach where an analyst estimated spread direction based on the sequential shift and expansion of each curve sequence, for the same points used for the normal direction vectors (referred to as Visual trend in Table 4)

ROS estimates were based on the linear distance of each fire spread vector divided by the time interval between image frame capture. Image capture times are recorded in the FireMapper 2.0 metadata.

We generated buffers around fire spread vectors to create rectangular analytical units for extracting topographic and fuel datasets for examining relationships with ROS. Similar to the spacing of fire spread vectors along fire front curves, selection of buffer widths was based on both theoretical and empirical grounds. Ideally, when assessing landscape controls on fire spread, buffer widths should be narrow, to sample specific portions of the landscape over which a fire actually spread. However, the actual path of fire spread is uncertain and not necessarily along straight lines normal to the time = *n* front location. Thus, the greater the uncertainty in spread direction the wider should be the buffer around a spread vector. We experimented with buffer widths of 30 m, 50 m, and 100 m for the Detwiler Fire to assess whether landscape variable statistics were sensitive to such variations.

4. Results

We present the results of the uncertainty analysis for estimating fire ROS, frequency distributions of ROS estimates for the three wildfires of opportunity, and descriptive/

graphical relationships between ROS and landscape covariates. We emphasize results for the Detwiler fire because the image time series associated with that fire event is more robust.

4.1. *Uncertainty of ROS estimates*

The nominal ground sampling distances (GSD) of FireMapper 2.0 imagery for the Cedar, Detwiler and Rey fires are 11 m, 13 m, and 13 m, respectively. We estimate the RMSE co-registration for image pairs used to estimate ROS to be 0.43, 0.30, and 0.32 pixels, respectively, as shown in Table 1. The overall average RMSE product for all three fires is 0.33 pixels or the equivalent of 4.13 m. These results are encouraging, suggesting that error and uncertainty of ROS estimates due to misregistration appear to be minor.

A fire front consists of very active combustion at the interface with unignited fuel, trailed by regions of non-continuous residual combustion and smouldering woody material, and hot ground and ash with an absence of flaming activity. Flames in natural vegetation have lengths that may range from one to a few metresin grasses to several tens of metres in chaparral. These often extend from the combustion zone to over the unignited fuel ahead of the spreading fire, depending on local winds. With an unaided eye, an observer perceives the fire by the visible-light emissions from hot, glowing soot particles within the flame; these emissions decline abruptly as the particulates rise and cool. Thus, we perceive a defined flame length. By contrast, thermal infrared emissions do not decline abruptly with decreasing particulate temperatures, so a well-defined flame length is not detected. Within the flaming combustion zone, thermal emissions from hot ground and fuels, which are spatially continuous and of high emissivity, actually exceed those of the flames, which are optically thin and of low emissivity. Thus, nadir views from a thermal imager will map the greatest emissions from hot ground beneath intense flames. Ahead of the combustion zone will be observed a gradient of declining emissions from flames reaching over unignited fuels.

Delineating the positions of successive fire front locations is another source of uncertainty. Such delineation is based on defining and adhering to rules for what constitutes the leading edge of an active fire front and faithfully and consistently delineating changing positions of leading edges. Active front delineations based on all four image analysis approaches for seven different image passes are shown in Figure 2. Also shown in Figure 2 are several temperature profiles selected to illustrate where each of the front delineation approaches typically intersected the profile and the spatial structure of radiant temperature in the active fire zone. Fronts delineated by all of these approaches tended to be located near the asymptote of the steep temperature decline from the peak apparent surface temperature, as discussed later in this article. We tested the four front delineation approaches for the seven-image sequence of the

Table 1. Misregistration error assessment for time sequential ATIR image pairs.

Fire Event	GSD (m)	# Test Points	RMSE (pixels)	RMSE (m)
Cedar	11	19	0.42	4.62
Detwiler	13	43	0.30	3.90
Rey	13	26	0.32	4.16
All three fires	-	88	0.33	4.13

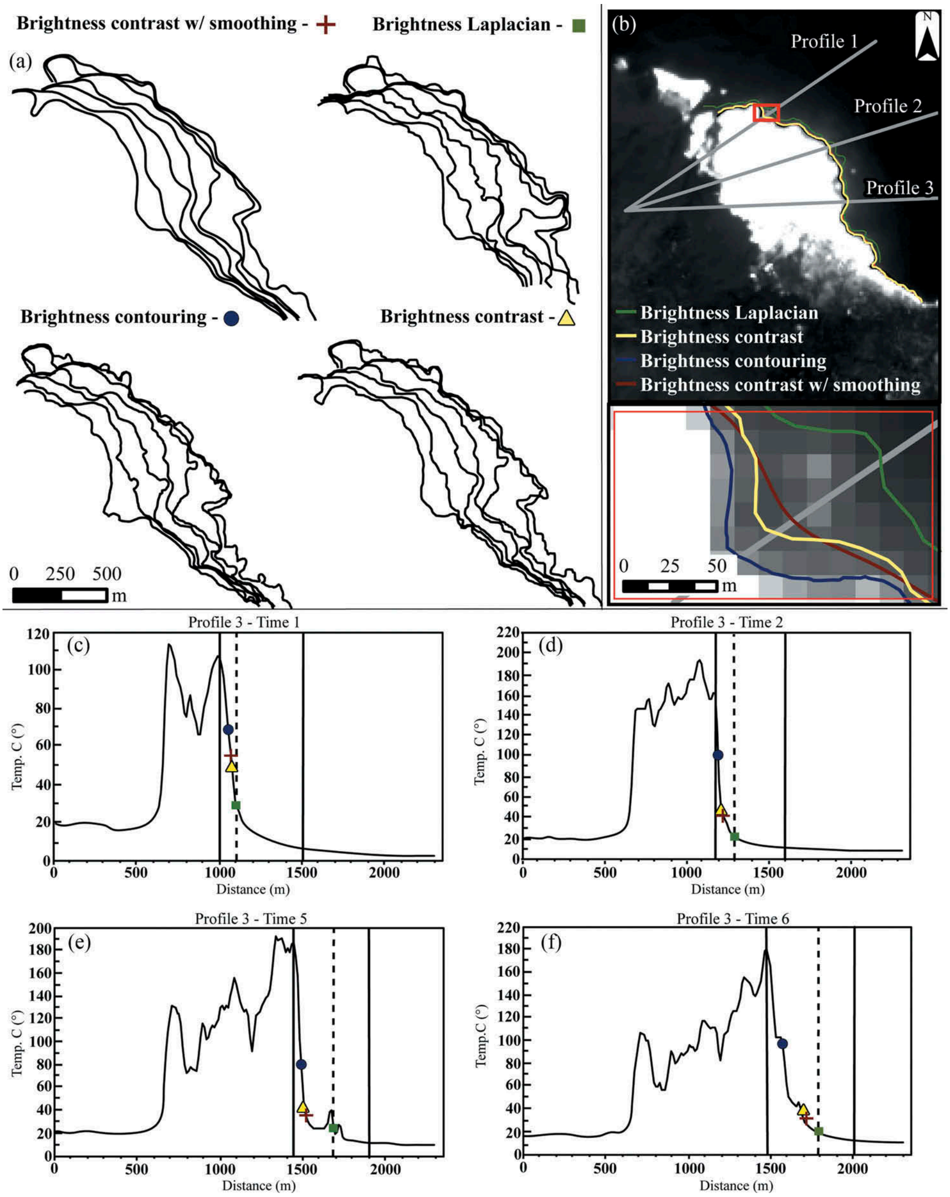

Figure 2. Comparison of active front delineations. (a) Positions of active fire front locations delineated with four different image enhancement approaches for a seven-image sequence of the Detwiler Fire captured 20 July 2017. (b) TIR image with front delineation methods and inset map (c–f) Apparent surface temperature profiles for several transects oriented mostly in the spread direction, with points at which delineated fire front positions marked.

Detwiler fire, by computing the relative, pairwise offset of active front positions and by comparing ROS estimates. The range and median statistics of multiple mean difference (MD) values for all seven active front positions combined were computed for pairs of three of the four curve delineations, as shown in Table 2. The positions of fire fronts from the different delineation approaches differed by a range of 21–51 m, with median MD

Table 2. Mean absolute difference (MD) statistics for positional offsets between pairs of delineated fire front curves for seven ATIR images of a portion of the Detwiler Fire.

Pairs of Front Delineation Approaches	Range MD (m)	Median MD (m)
Brightness contrast vs. Contour	20.29–29.27	25.79
Brightness contrast vs. Laplacian	33.01–39.36	35.56
Contour vs. Laplacian	39.39–51.25	42.69

varying between 26 and 43 m. The most similar front positions were delineated based on brightness contrast and contouring enhancements and the most dissimilar positions with the contouring and Laplacian enhancements. Though front positions differed by approach, each yielded similar ROS estimates, when using a normal spread vector extending from the earlier time front (Table 3). The greatest difference in average and median ROS for all six successive time intervals between any two front delineation approaches (contrast stretch with manual vs. Laplacian filter) is less than 8% of the average ROS magnitude. The greatest difference for any successive image pair is 22% for the same two approaches. These results suggest that consistency in implementing an enhancement and manual front delineation approach is more important than which enhancement is used and imply that potential interpreter bias may not be an important factor, or at least can be overcome.

We also evaluated uncertainty in ROS estimates associated with measuring spread vector distances for the Detwiler fire sequence, which result from differences in

Table 3. Comparison of fire rate of spread estimates based on different active front delineation approaches for a seven-image sequence of the Detwiler Fire.

		ROS Estimates (m min^{-1})				
Time Step (Elapsed Time)	ATIR Image Enhancement Approach	Min	Max	Range	Average	Std. Dev
1–2 (7:22 min)	Brightness contrast	0.75	21.64	20.89	7.33	5.80
	Brightness contrast w/smoothing	2.05	20.02	17.97	8.03	5.75
	Brightness contouring	1.79	24.11	22.32	8.88	5.36
	Laplacian	1.45	20.60	19.15	8.73	5.53
2–3 (7:34 min)	Brightness contrast	0.61	21.52	20.91	7.85	6.26
	Brightness contrast w/smoothing	1.03	21.48	20.45	8.46	5.86
	Brightness contouring	0.48	21.48	22.56	8.74	6.27
	Laplacian	1.80	24.82	23.01	9.86	6.15
3–4 (8:04 min)	Brightness contrast	1.47	12.10	10.63	7.39	3.42
	Brightness contrast w/smoothing	1.26	13.43	12.17	8.02	3.14
	Brightness contouring	0.64	14.42	13.79	7.34	4.58
	Laplacian	0.75	18.24	17.49	7.77	4.63
4–5 (8:16 min)	Brightness contrast	1.76	20.13	18.38	7.83	5.10
	Brightness contrast w/smoothing	2.63	16.74	14.11	8.39	4.61
	Brightness contouring	1.32	20.81	19.49	7.85	5.49
	Laplacian	1.59	20.65	19.06	8.85	6.59
5–6 (8:45 min)	Brightness contrast	0.60	36.94	36.33	7.61	9.56
	Brightness contrast w/smoothing	0.74	37.37	36.63	7.41	9.33
	Brightness contouring	0.57	29.06	28.49	6.97	7.40
	Brightness Laplacian	1.89	38.42	36.53	7.62	8.49
6–7 (8:42 min)	Brightness contrast	0.39	14.68	14.29	4.83	4.56
	Brightness contrast w/smoothing	0.63	12.72	12.10	4.93	4.03
	Brightness contouring	0.40	13.36	19.96	4.42	3.93
	Laplacian	0.75	9.29	8.54	3.69	2.77
		Cumulative ROS Measurements				
	Brightness contrast	0.39	36.54	36.54	7.08	50.83
	Brightness contrast w/smoothing	0.63	37.37	36.74	7.44	46.13
	Brightness contouring	0.40	29.06	28.66	7.29	47.19
	Laplacian	0.47	38.42	37.68	7.65	47.98

approaches to delineating these vectors between successive front curves. As shown in Table 4, differences between ROS estimates based on each spread vector approach are generally small. The greatest difference in average ROS for all six successive image pairs combined between any two front delineation approaches (6.316 m min^{-1} vs 6.840 m min^{-1}) is less than 8% of the average ROS magnitudes. The greatest difference between two approaches for any single time interval is 15% of the average ROS magnitude. Decreasing the spacing between normal vectors by a factor of two (i.e. twice the spatial frequency) decreased the overall average ROS by around 7% and yielded lower ROS estimates for all but one of the six time intervals.

Temporal uncertainty of ROS estimates pertains to recording the time the image frame was acquired. Time of acquisition is determined by an onboard computer's clock that controls camera triggering and image data storage. Since the important temporal variable is the time interval between repetitive image frames, relative errors in time coding are minimal (<1 s).

4.2. *Detwiler Fire*

The seven-image sequence for the Detwiler Fire (Figure 3) captures more fire spread dynamics than the other two wildfires for which repetitive imagery was captured for this study. During the time-sequential imaging, the fire primarily spread downslope in

Table 4. Comparison of fire rate of spread estimates based on different spread vector delineations approaches for a seven-image sequence of the Detwiler Fire.

Time Step (elapsed time)	Spread Vector Approach	Rate of Spread Estimates (m min^{-1})					
		Min	Max	Range	Median	Average	Std. Dev
1–2 (7:22 min)	Normal to curve – wider spacing	1.68	19.94	18.27	5.24	7.23	5.64
	Normal to curve – closer spacing	1.17	19.78	18.61	3.95	6.82	5.57
	Normal to trend	1.40	19.36	17.96	3.79	6.65	5.54
	Visual trend	1.71	20.51	18.80	3.96	7.16	5.92
2–3 (7:34 min)	Normal to curve – wider spacing	0.88	21.87	20.99	5.37	7.73	6.34
	Normal to curve – closer spacing	0.83	20.92	20.04	5.08	7.54	6.05
	Normal to trend	1.17	20.38	19.21	5.17	7.68	6.26
	Visual trend	0.88	21.85	20.97	5.95	7.83	6.32
3–4 (8:04 min)	Normal to curve – wider spacing	1.11	12.61	11.47	6.43	6.87	3.51
	Normal to curve – closer spacing	0.70	12.61	11.91	7.44	6.90	3.54
	Normal to trend	1.12	12.69	11.57	7.41	7.01	3.43
	Visual trend	1.13	13.63	12.50	8.35	7.40	3.58
4–5 (8:16 min)	Normal to curve – wider spacing	1.19	18.25	17.06	6.27	7.66	5.01
	Normal to curve – closer spacing	0.35	16.91	16.56	5.61	7.10	4.46
	Normal to trend	1.56	15.16	13.59	6.21	6.98	4.30
	Visual trend	2.41	18.30	15.89	6.86	7.62	4.41
5–6 (8:45 min)	Normal to curve – wider spacing	0.30	30.97	30.67	3.72	7.79	8.70
	Normal to curve – closer spacing	0.29	28.68	28.40	3.57	6.44	7.47
	Normal to trend	0.31	23.59	23.65	3.70	7.01	7.75
	Visual trend	0.33	26.86	26.53	3.73	7.55	8.19
6–7 (8:42 min)	Normal to curve – wider spacing	0.51	12.76	12.25	2.85	3.90	3.44
	Normal to curve – closer spacing	0.54	12.47	11.93	2.65	3.71	3.24
	Normal to trend	0.78	11.83	11.05	2.61	4.04	3.42
	Visual trend	0.52	13.09	12.57	3.01	4.08	3.42
		Cumulative ROS Measurements					
	Normal to curve – wider spacing	0.30	30.97	30.67	4.62	6.80	5.80
	Normal to curve – closer spacing	0.29	28.68	28.40	4.38	6.32	5.38
	Normal to trend	0.31	23.95	23.65	4.68	6.51	5.40
	Visual trend	0.33	26.86	26.53	4.74	6.84	5.62

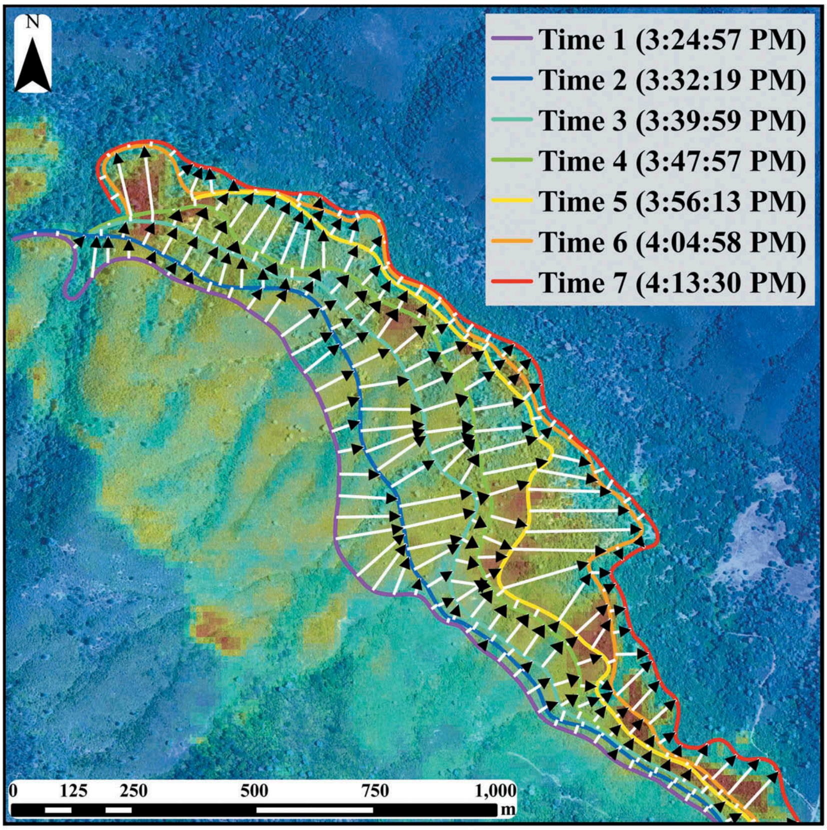

Figure 3. Fire spread sequence for Detwiler Fire. Active fire fronts and fire spread vectors are portrayed for the seven-image sequence on 20 July 2017. The background image is a fusion of NAIP colour (depicting vegetation fuels and topography) with a colour density sliced version of the seventh FireMapper 2.0 image.

a westerly direction, shown in Figure 4(a). Average wind speeds from the nearest weather station (13 km away) were recorded at 5 m s^{-1} (peak gusts 8 m s^{-1}) prevailing from the WSW at the time of the imaging. Fuels on the east facing slope were composed primarily of shrubs and trees with progressively greater tree composition near the lower reaches of the slope, as depicted in Figure 3. The fire spread at a uniform average rate between 7 and 9 m min^{-1} for the first five time intervals and then slowed to an average of about 4 m min^{-1} during the last (sixth) time interval. However, the range of ROS for individual portions of the fire ranged between 0.4 and 40 m min^{-1} for the 6–8 min repeat intervals throughout the 49 min period of sequential TIR imaging, as shown in Tables 3 and 4. Indications that the fire spread slower within topographic depressions composed mostly of dense trees is visually apparent when overlaying delineated fire front curves and spread vectors on the high spatial resolution NAIP imagery, as seen in Figure 3.

Figure 4 depicts maps of variables that are likely associated with ROS for the Detwiler fire spread study area, with varying sampling buffer widths plotted to illustrate differences in their sizes and sampling characteristics. An NDVI image with 30 m wide

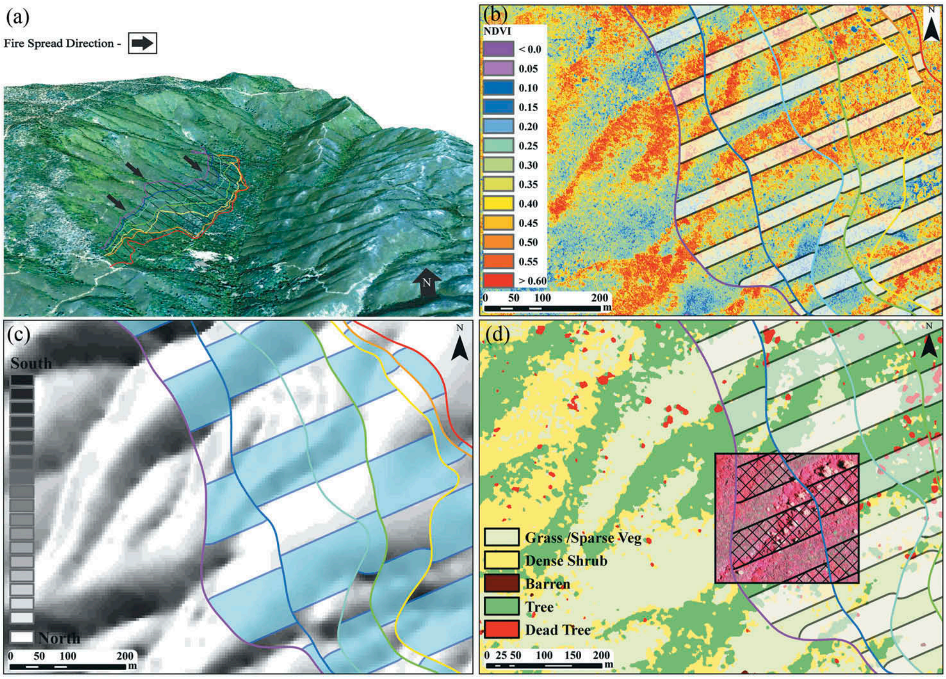

Figure 4. Detwiler Fire spread, landscape covariates, and different sampling buffer widths. (a) 3-D perspective image depicting active fire front and spread vectors. (b) Colour-slice version of a normalized difference vegetation index (NDVI) image, with 30 m wide sampling buffers associated with fire spread vectors. (c) Slope aspect map with 50 m buffers. (d) Vegetation fuel type map with 100 m buffers.

sampling buffers is portrayed in Figure 4(b). Since NDVI is a readily derived indicator of the amount of above ground green vegetation material, it spatially represents the relative amount of vegetation fuel as it tends to co-vary with vegetation composition, structure and mass (Myneni 1995; Uyeda, Stow, and Riggan 2015). A slope 'northness' map with 50 m buffers is shown in Figure 4(c). Figure 4(d) contains a map of vegetation growth form and cover types with 100 m buffers around spread vectors depicted. Fractional cover of growth forms (e.g. shrubs or trees), tree mortality, or barren cover can be extracted from buffer areas on the map and examined as covariates. As a form of slope aspect, northness suppresses the circularity effect associated with degrees of aspect and can be used directly (along with 'eastness') maps as continuous variables in landscape covariates analysis.

Relationships between ROS and NDVI as a landscape covariate and effects of varying buffer widths are illustrated in Figure 5. Examples of fire spread roses depicting frequencies of ROS occurrence in 16 different directional sectors (Figure 5(a–d)) illustrate that the fire primarily spread to the northeast with the fastest moving portions spreading directly to the east. Differential sampling effects from using different buffer sizes and spacing appear to be negligible. Histograms of ROS as a function of NDVI for different buffer sizes in Figure 5(e–i) show that the frequency distributions for different buffer widths are similar.

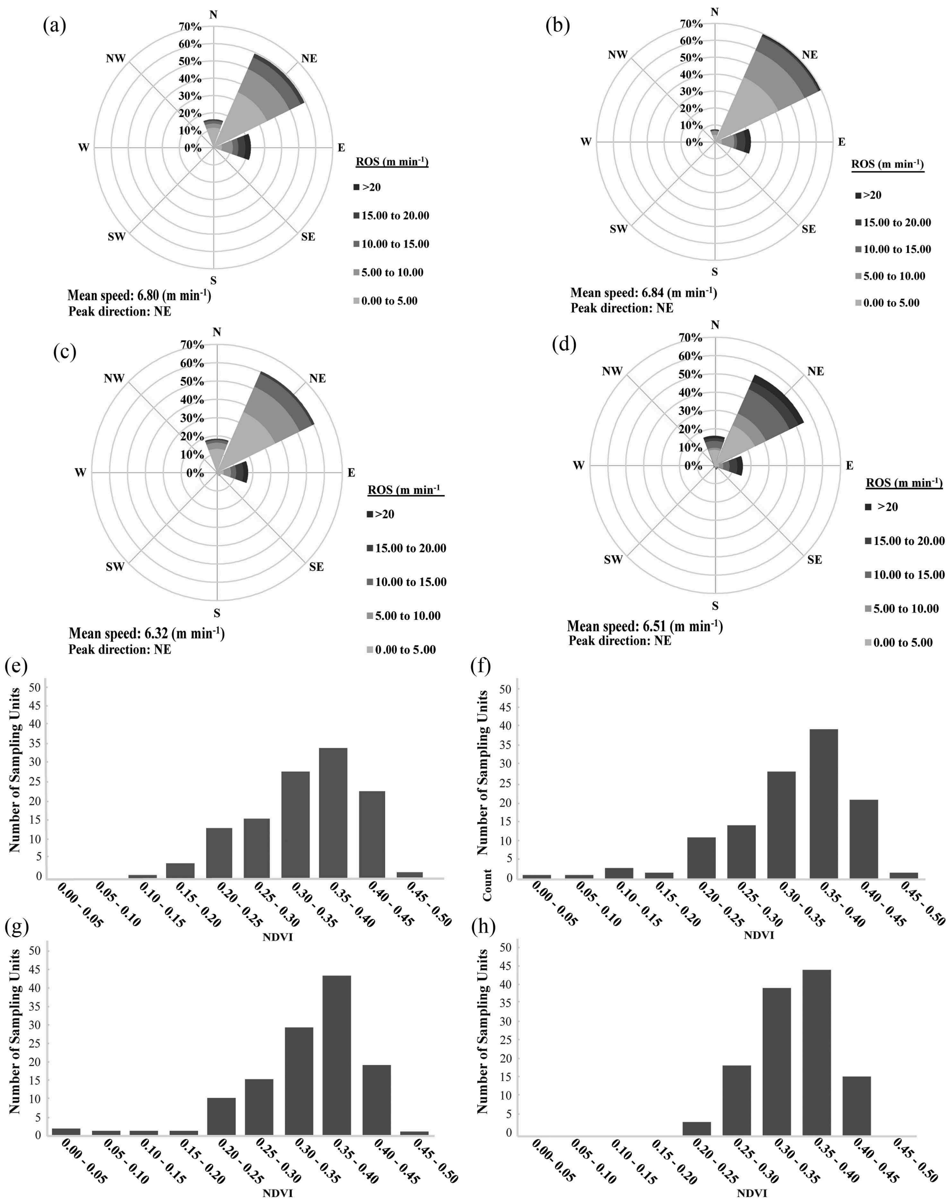

Figure 5. Comparison of fire spread roses and histograms for different buffer sizes for the Detwiler Fire (20 July 2017). (a) Fire ROS rose based on spread vectors with no buffer. (b) Fire ROS rose based on 30 m wide buffers. (c) ROS rose based on 50 m buffers. (d) ROS rose based on 100 m buffers. (e) NDVI histograms derived from spread vectors with no buffer. (f) NDVI histograms derived from 30 m wide buffers. (g) NDVI histograms derived from 50 m buffers. (h) NDVI histograms derived from 100 m buffers. Histograms in (e) through (h) portray the mean NDVI value for all pixels within the spread vector or buffer zone sampling units.

4.3. *Cedar Fire*

Similar to the Detwiler Fire, the Cedar Fire of August 2016 occurred on the Sierra Nevada foothills of Kern County, California and burned through a mix of woodland, shrubland

and grassland vegetation. Only a single segment of the slow-moving backing (against the predominant wind direction and fire spread) was covered with repetitive ATIR imagery with two imaging passes occurring more than 18 hours apart, as shown in Figure 6. However, this relatively long time interval is reasonable and appropriate for tracking a slow-spreading segment of a fire and enables estimates of ROS when fuel and topography conditions are dominant (i.e. wind influences are negligible).

Fire front and spread vector delineations for the study segment of the Cedar Fire are shown in Figure 6(b–d). ROS estimates for the backing fire ranged from 7 to 17 m min^{-1} with an average spread of 11 m min^{-1}. This section of the fire burned both upslope and downslope, as observed from Figures 6(d and e). The joyplots in Figure 6(f-g) show how the fire spread faster upslope than downslope. In Figure 6(f) one can see how the faster moving segments occurred in areas with higher median NDVI values, suggesting higher amounts of fuel. However, it may be the case that the fire moved faster going upslope and those slopes tended to have greater amounts of green vegetation (and therefore, higher NDVI values).

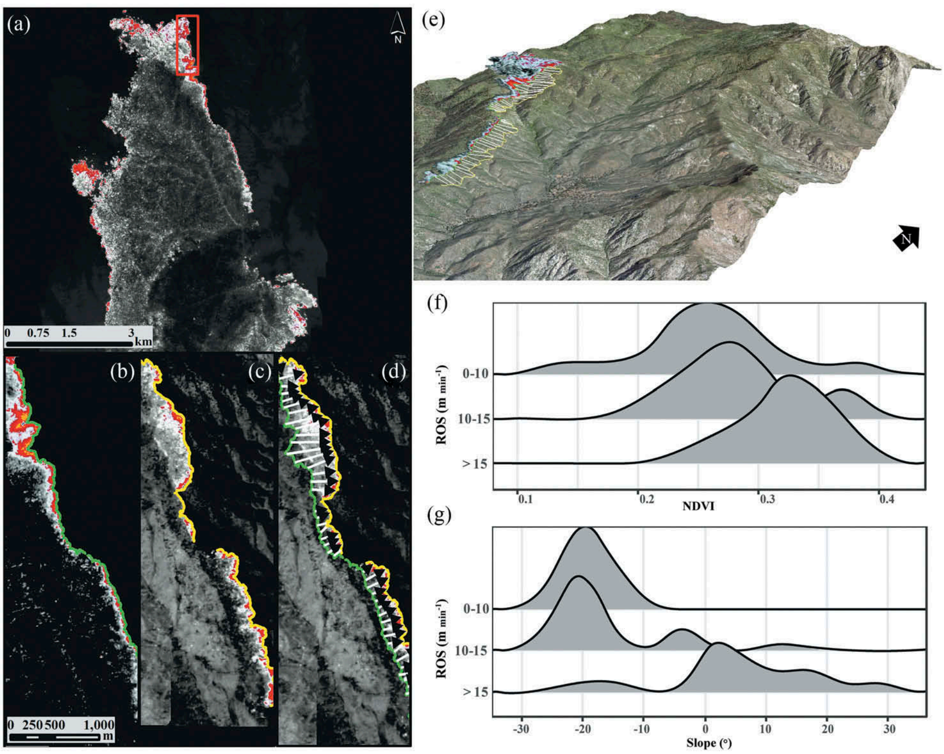

Figure 6. Wildfire spread during the Cedar Fire on 19 August 2016. (a) TIR image mosaic showing fire perimeter on 19 August 2016 and subset of backing fire front. (b) Time 1 backing fire front. (c) Time 2 backing fire front (18 hrs 31 mins later). (d) Active fire fronts and delineated fire spread vectors. (e) 3-D perspective image depicting active fire front and spread vectors. (f) Joy plots for ROS for three ranges of NDVI values. (g) Joy plots for ROS for three ranges of slope angles; positive slopes associated with upslope fire spread and negative downslope.

4.4. *Rey Fire*

Also in August 2016, the Rey fire burned through mountainous chaparral in Santa Barbara, County, California. A sequential pair of images captured 7 min apart on 21 August 2016 enabled ROS estimates of a fast-moving fire, as shown in Figure 7. During this brief period, the fire spread through steep terrain. ROS estimates range between 7 and 49 m min^{-1} with a mean rate of 25 m min^{-1}, primarily to the southeast. Average wind speeds from the nearest weather station 19 km were recorded at 2 m s^{-1} (peak gusts 7 m s^{-1}) prevailing from the west at the time of the imaging.

5. Discussion

5.1. *Theoretical elements of ROS estimation*

Making reliable estimates of wildfire ROS with repetitive ATIR imagery at spatial scales on order of 5–500 m and time scales of 5–50 min is challenging. Wildfires spread by pre-heating, pyrolysis, and subsequent combustion of gaseous fuels, followed by the burning of char, and through the transfer of heat to and contact of flames with fuels (Finney et al. 2010). Estimating fire spread rates is different than estimating fluid or particle flow

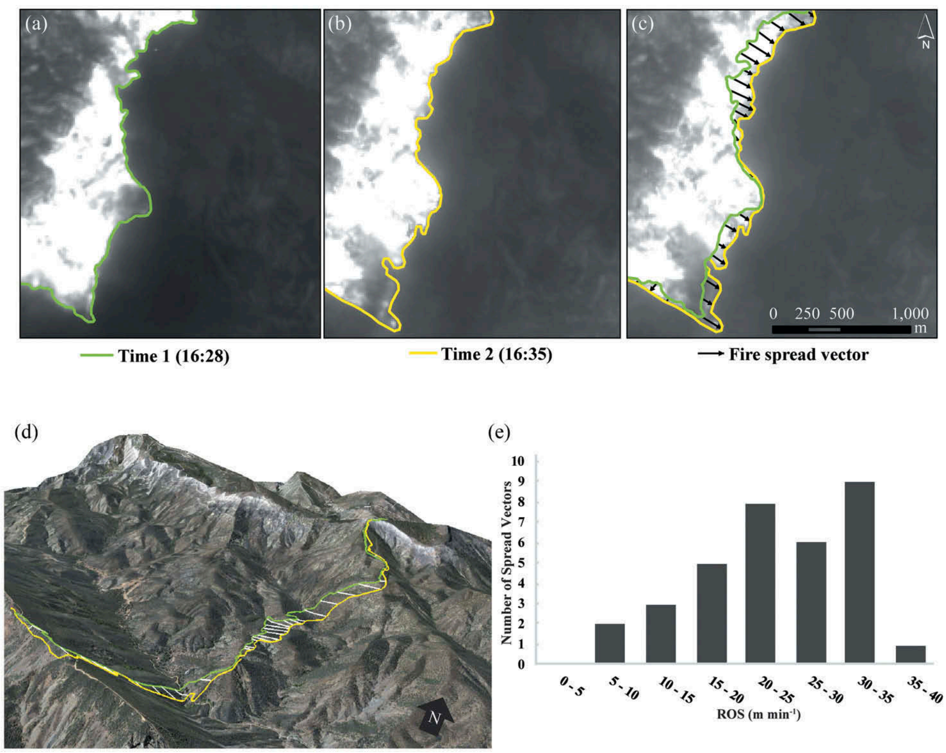

Figure 7. Wildfire spread during the Rey Fire on 21 August 2016. (a) Time 1 fire front. (b) Time 2 fire front (7 min later). (c) Fire spread vectors and ROS statistics. (d) 3-D perspective image depicting active fire front and spread vectors. (e) Histogram depicting frequency distribution of ROS estimates for all spread vectors in the two-pass imaging sequence.

rates. In the latter, discrete matter can be considered traceable points within the fluid medium. Tracking and measuring the advancement of active fire fronts is more challenging as fronts are generally considered to be curvilinear one-dimensional features. The path of fire spread at shorter space and time scales is more stochastic, depending on localized wind movements, terrain facets, and heterogeneous fuel conditions. In addition, when image capture occurs every 5–50 minutes – a typical interval for airborne data where aircraft must revisit the fire for another look – it is impossible to unambiguously reconstruct the exact path that particular portions of a wildfire's leading edge took at shorter time scales. This leads to the common assumption of a likely constant or mean path and direction of movement, based on the spatial patterns of sequential fire front locations and/or on fire spread theory. In fire spread modelling, level set theory often guides model simulations of the expansion of fire perimeters (Mallet, Keyes, and Fendell 2009; Lautenberger 2013). Associated with this theory is the assumption that fire perimeters advance in a normal (perpendicular) direction from the most recent perimeter (fire front) location. However, in reality, shifts in wind direction or changes in orientations of topographic slopes may drive the spread of a fire in a direction that is different than the normal to a prior front location, particularly when observing at shorter time intervals. In fire spread modelling, ROS is typically calculated using the component of wind velocity and terrain gradient that is normal to the fire line at points along the fire line. However, in our case, we seek to estimate direction and magnitude of ROS independent of wind and terrain data, to enable independent statistical or graphical evaluation of their influences on ROS. In the absence of wind and topographic information, the only information guiding estimation of spread vectors is the change in form of sequential fronts, and the spatial pattern of image intensities that primarily represent the spatial distribution of surface temperatures.

Of the factors influencing error and uncertainty in ROS estimates, delineation of active fire front positions and spread vectors were deemed to be the most important. In this study, longwave (8–12 μm) TIR imagery used to estimate ROS mostly portrays spatial variations in ground surface temperatures (Allison et al. 2016; O'Brien et al. 2016). In the active fire zone, heat from a fire is imparted to the ground with the flame zone and burning fuels being mostly transparent, meaning that they have lower emissivity values and apparent surface temperatures (Johnston, Wooster, and Lynham 2014; Johnston et al. 2018). For the Detwiler Fire sequence, this flaming zone just behind the fire front location is observed on surface temperature profiles as zone of rapid temperature decline ranging between 235 and 540 m (with a mean of 340 m) on the ground. Hot soot and gases in and downwind from the active fire front location also exhibit radiant temperatures that are warmer than ambient land surface temperatures but cooler than the fire heated ground surface and flaming zones (Johnston et al. 2018). Thus, the edge or highest spatial gradient of radiant temperature on TIR images – normally delineated as the location of an active fire front – is associated with the location where ground temperature from the fire is high, emissivity is lower from the presence of flames, and cooler surfaces not yet heated from the fire are adjacent in the spread direction. Ahead of the front location is a shallow gradient from the warmed gases and soot in advance of the flame front until ambient temperatures are reached. Assuming that this ground-to-image gradient relationship is consistent between images captured sequentially over time, the key is to delineate fire front locations on each image in a consistent manner. As we demonstrate in the Results section, manual, automated, and hybrid approaches to delineating fire front locations yielded different representations of the front but when applied in a consistent manner, yielded similar ROS estimates.

Assuming that spread vectors are represented as straight line features, the main considerations for their delineation are (1) origin, (2) spacing, and (3) direction. *Origin* is the point on either the time = n or time = n + 1 active front curve from which the vector emanates; typically and most realistically, origin points lie on the time = n front. *Spacing* is the regular or random interval distance between origin points. Regularly spaced intervals starting from a random location near the end of an active fire front segment can be selected automatically and should be unbiased. Manual selection with a minimum spacing criterion can ensure estimates at critical points along the front curve but can introduce interpreter bias. Automatic delineations based on algorithms of sequential image processing steps may be less biased but are sensitive to discontinuities and irregularities in the image brightness fields, which can yield inaccurate front positions (Ononye, Vodacek, and Saber 2007; Valero et al. 2018). *Direction* is the angular orientation of the linear vector emanating from an origin point. As tested and summarized in the Results section, direction can be automatically delineated as the normal from the origin point on an (typically earlier-time) active front curve or automatically or interactively delineated in the general trend direction of the fire spread. This general trend direction may conform with the prevailing wind direction at the time of the active front passage. Isolated, higher frequency spread features may move in directions different than normal to the origin or the general spread trend, which could bias ROS estimates for those features. This bias may be minimized by incorporating topographic and wind data as part of the spread vector delineation process. However, as mentioned previously, this would preclude the independent evaluation of forcing (covariates analysis) of ROS by wind or topographic variables.

The appropriate approach for locating fire spread vectors, summarizing ROS, and/or exploring relationships with landscape covariates depends on the rationale or application for making such estimates. For fire behaviour studies or validation of fire spread model simulations, frequency distributions of ROS for different segments of a fire perimeter characterize variability of fire spread within and between specific fire segments of a fire perimeter. Maximum and median ROS extracted from frequency distribution data may be particularly informative for these applications. When attempting to understand landscape controls on ROS, fire spread vectors may be sampled from within fire spread units (features along the fire perimeter exhibiting characteristic patterns of fire spread), topographic slope facets (land units having nearly constant slope angle and aspect), fuel patches (land units with homogenous vegetation and/or non-vegetative cover fuel characteristics), or integrated landscape units (land units associated both with homogeneous topographic and fuel characteristics). Fire ecologists may be more interested in fire residence times (inversely proportional to ROS) and fire intensities, in addition to landscape controls on ROS (Keeley, Brennan, and Pfaff 2008). Fire suppression and emergency response managers could benefit most from maximum and median ROS for the most rapidly advancing portion of a fire perimeter, as well as for locations where firefighters or rural dwellers are particularly vulnerable. This would require a mostly automated, near real-time imaging and processing capability, possibly linked with fire simulation modelling (Valero et al. 2017).

5.2. *Scale and sampling considerations*

Estimating the rate and direction of wildfire spread for time-sequential ATIR imagery is scale dependent and influenced by sampling opportunity and effort. Wildfires generally ignite in a non-predictable manner, both in terms of location and time. To capture time sequential ATIR imagery for a wildfire event requires knowledge of occurrence and location of fire ignition and then for an aerial imaging system to be mobilized and transit to the fire location. While en route, weather data and fire detection maps based on Moderate Resolution Imaging Spectro-radiometer (MODIS) or Visible Infrared Imaging Radiometer Suite (VIIRS) satellite TIR data may be accessed to provide initial situational awareness for flight planning. Once over a fire, pilot and sensor operator assess the perimeter extent and location of the most active fire front, based on smoke plumes, flame presence and height (if visible), and/or presence of vertically developed clouds. These indicators may guide location of initial TIR imaging, with these initial images allowing the operator to detect the active fire and establish the location of the first flight line for repetitive imaging passes. This repetitive capture approach can be achieved with a racetrack flying pattern, with the imaging pass along one length of the racetrack, oriented primarily perpendicular to the predominant fire spread direction, as shown in Figure 8. Ideally, TIR image station positions are recorded on the first pass and imaging frames are captured at nearly the same imaging stations using a global navigation satellite system (GNSS) based triggering system. This enables view geometry to be replicated and image registration to be

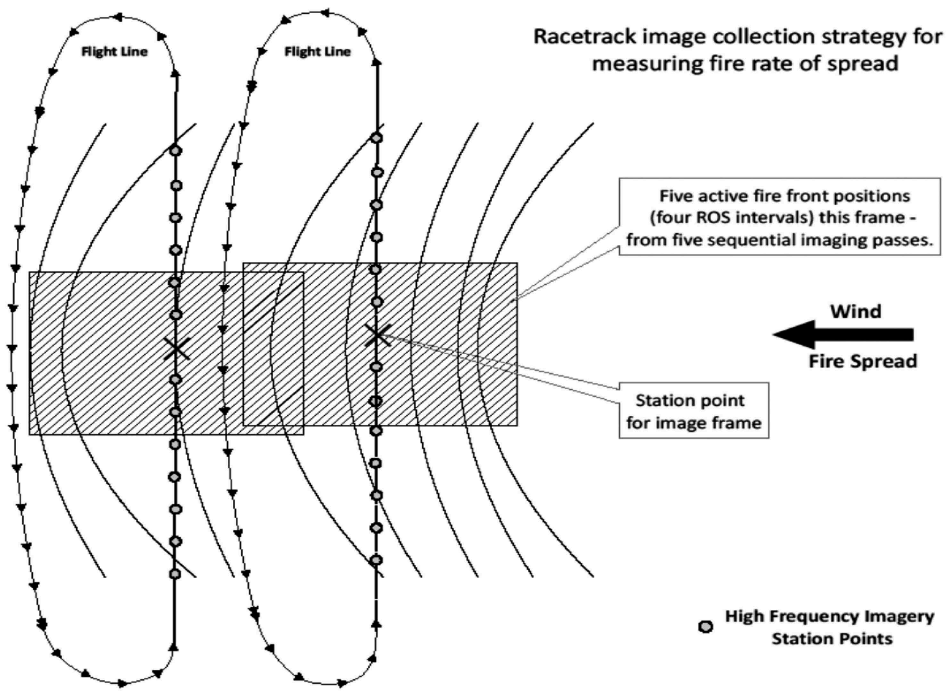

Figure 8. Ideal aerial image capture pattern. A racetrack flying pattern with repeated imaging stations is illustrated. An aircraft repeats the same flight pattern and TIR sensor captures images repetitively at the same imaging stations based on GPS triggering systems. Once the active front location is close to falling outside of image frames, a new racetrack pattern is established in the direction of the fire spread.

more accurate, through an approach known as repeat station imaging (Coulter, Stow, and Baer 2003; Stow et al. 2016). The racetrack imaging pattern is repeated until the sensor operator determines that the active fire front is near the down-spread edge of an image frame. A new imaging flight line and associated racetrack pattern is established in the direction of the fire spread, such that the active fire front is imaged in the up-spread direction of the image frame. Sequential imaging is repeated as above. The imaging mission described in this paragraph represents an ideal approach that is informed by our experiences with the three fire events examined in this study.

While the ATIR imaging approach described and evaluated in this study enables science-based measurement of ROS and analysis of fire behaviour at spatial and temporal scales not generally attempted in the past, resultant data and knowledge depend on the random nature of wildfires of opportunity, their behaviours and what specific area burns during imaging period. The influence of sampling specifications on ROS estimates primarily pertain to which portion of the fire perimeter is imaged and the temporal repeat frequency of imaging. The most active portion of the fire front, normally at the down-wind furthest extent of the perimeter, is likely to be the most dynamic and therefore, the area of imaging emphasis. The critical repeat interval is dependent on the magnitude of ROS and uncertainty in its measurement. A rule of thumb for imaging repeat interval (ΔT_{min}) is derived in Equation 1:

$$\Delta T_{\text{min}} = k \times \text{ROS}/\text{GSD} \tag{1}$$

where k accounts for uncertainty in numbers of pixels for image registration and delineations of active front positions and spread vectors. Since ROS is unknown and the variable to be estimated, some estimate of the general rate of perimeter expansion from prior observations could be used to establish ΔT_{min}. However, imaging the same flight line as frequently as is feasible (determined by the total length of the racetrack pattern and aircraft ground speed) is desirable. Even if the temporal frequency is too high (i.e. $\Delta T < \Delta T_{\text{min}}$) to justify front and spread vector delineation between every repeated image pair (i.e. spread distance just a few pixels), higher frequency observations can visually inform a more reliable determination of the spread direction between delineated fire fronts. The longer the repeat interval relative to the ROS, the greater the potential for spread vectors to be associated with multiple terrain slope facets, rendering such ROS samples useless when examining the influence of terrain slope.

Whether characterizing the frequency distribution of ROS for portions of a wildfire or conducting statistical analyses of landscape controls on ROS, the spacing between spread vectors and the width of buffers for sampling landscape variables in the vicinity of such vectors are important sampling considerations. Selecting the spacing between spread vectors involves a trade-off between measurement and statistical independence and adequately sampling the dynamics of fire spread and the landscape that partially controls such spread. Uncertainty in the path of fire spread between imaging periods and the objective to maintain independence is rationale for selecting a large spacing distance. Complexity in the form of fire front curves and fine-scale spatial variability in ROS suggests a need for more tightly spaced vectors, as do landscapes with heterogeneous fuel and topographic distributions. The appropriate width of buffers around spread vectors used to sample fuel and topographic data for landscape covariates analysis similarly depends on the uncertainty of the spread path and influences statistical independence. Narrower buffer widths are more likely to represent only the fuel and topographic conditions through which the specific portion of a fire spread, assuming a linear path between successive front positions, and are more likely to achieve statistical independence. Wider buffer widths better account for uncertainty in spread path but are more likely to be too close to or even overlap with adjacent buffers, increasing the potential for spatial dependence. Results from our limited empirical evaluation of spread vector spacing and buffer width suggest that decreasing the spread vector spacing by a factor of 2 yielded ROS estimates that were slightly and consistently less than when the spacing was wider. Also, buffer widths of 30 and 50 m yielded similar histograms for landscape covariate metrics, and substantially different than when 100 m buffers were implemented.

5.3. *Findings from three wildfires of opportunity*

ATIR image sequences for the Cedar, Detwiler, and Rey Fires enabled observations of a range of fire behaviours and landscape conditions, even though the capture approaches are less than ideal and datasets are limited in spatial extent and temporal coverage. Cedar and Detwiler Fires burned in landscapes typical of the Sierra Nevada foothills, within rolling terrain and a mixture of shrubland and woodland vegetation. The long (18.5 hr) interval between passes for the Cedar Fire image pair is suitable for ROS estimates of the backing portion of a fire perimeter, capturing the fire as it moved downslope. ROS ranged between 7 and 17 m min^{-1}, with an average ROS of 11 m min^{-1}. The seven-image sequence of the Detwiler Fire also captured a fire spreading downslope and in similar fuel types but along the active flank of the fire. ROS estimates for this portion of the Detwiler Fire are similar to those of the backing portion of the Cedar Fire, with an average spread of 8 m min^{-1}. Of the three study fires, the fastest spread rates (average spread of 25 m min^{-1} with maximum of 39 m min^{-1}) are estimated for the Rey Fire. The active front for the two-image pair captured for the Rey Fire burned in steep and irregular terrain, mostly through dense chaparral fuels. However, this single, short-interval image pair provides a limited sample of the Rey Fire behaviour.

Acknowledgements

ATIR image acquisition and pre-processing was conducted by Michaela Truman and David Maxwell of Kolob Canyon Air Services, Cedar City, UT. Lloyd (Pete) Coulter assisted with evaluation of image co-registration accuracy. Referees provided valuable recommendations for improving this article.

Disclosure statement

No potential conflict of interest was reported by the authors.

Funding

This research was funded by US National Science Foundation, Division of Social, Behavioural and Economic Research, Geography and Spatial Sciences program [grant no. G00011220]; and Directorate for Social, Behavioral and Economic Sciences.

ORCID

Douglas Stow http://orcid.org/0000-0001-5246-7073
Emanuel Storey http://orcid.org/0000-0001-8896-1444

References

Alexander, M., and M. Cruz. 2013. "Assessing the Effect of Foliar Moisture on the Spread Rate of Crown Fires." *International Journal of Wildland Fire* 22: 415–427. doi:10.1071/WF12008.

Allison, A., J. M. Johnston, G. Craig, and S. Jennings. 2016. "Airborne Optical and Thermal Remote Sensing for Wildfire Detection and Monitoring." *Sensors* 16 (1310): 29.

Barron, L., and M. Gajanan. 2018. "California's Wildfires Have Become Bigger, Deadlier, and More Costly Here's Why." Time Magazine, November 13.

Beyers, J., P. Riggan, D. Weise, T. Paysen, and M. Narog. 2007. "Age-Class Mosaics and Wind-Driven Fire: Further Fuel for the Debate." *USFS Project Number 07-1-2-10*.

Coulter, L., D. Stow, and S. Baer. 2003. "A Frame Center Matching Technique for Precise Registration of Multitemporal Airborne Frame Imagery: Methods and Software Approaches." *IEEE Transactions of Geoscience and Remote Sensing* 41: 2436–2444.

Cruz, M. G., M. E. Alexander, and A. L. Sullivan. 2017. "Mantras of Wildland Fire Behaviour Modelling: Facts or Fallacies?" *International Journal of Wildland Fire* 26: 973–981.

Finney, M. A., J. D. Cohen, I. C. Grenfell, and K. M. Yedinak. 2010. "An Examination of Fire Spread Thresholds in Discontinuous Fuel Beds." *International Journal of Wildland Fire* 2010 (19): 163–170.

FireMapper Tools ver. 3.4.2.258. 2009. *USDA Forest Service, Pacific Southwest Research Station, Forest Fire Laboratory, 4955 Canyon Crest Drive*, 92507. Riverside, California: US Department of Agriculture.

Ji, Y., J. T. Randerson, N. Faivre, S. Capps, A. Hall, and M. A. Goulden. 2014. "Contrasting Controls on Wildland Fires in Southern California during Periods with and without Santa Ana Winds. Journal of Geophysical Research." *Biogeosciences* 119: 432–450.

Johnston, J. M., M. J. Wheatley, M. J. Wooster, R. Paugam, G. M. Davies, and K. A. DeBoer. 2018. "Flame-Front Rate of Spread Estimates for Moderate Scale Experimental Fires are Strongly Influenced by Measurement Approach." *Fire* 1: 16–17.

Johnston, J. M., M. J. Wooster, and T. J. Lynham. 2014. "Experimental Confirmation of the MWIR and LWIR Grey Body Assumption for Vegetation Fire Flame Emissivity." *International Journal of Wildland Fire* 23: 463–479.

Keeley, J. E., T. Brennan, and A. H. Pfaff. 2008. "Fire Severity and Ecosystem Responses following Crown Fires in California Shrublands." *Ecological Applications* 18: 1530–1546.

Lautenberger, C. 2013. "Wildland Fire Modeling with an Eulearian Level Set Method and Automated Calibration." *Fire Safety Journal* 62: 289–298.

Leica Geosystems GIS and mapping. 2006. *ERDAS Imagine Tour Guides*. Atlanta: Leica Geosystems GIS and Mapping.

Loboda, T. V., and I. A. Csiszar. 2007. "Reconstruction of Fire Spread within Wildland Fire Events in Northern Eurasia from the MODIS Active Fire Product." *Global and Planetary Change* 56 (3–4): 258–273.

Loomis, I. November 29, 2018. "Communities of Color are More Vulnerable to Wildfires." *Eos* 99. doi:10.1029/2018EO110897.

Mallet, V., D. E. Keyes, and F. E. Fendell. 2009. "Modeling Wildland Fire Propagation with Level Set Methods." *Computers and Mathematics with Applications* 57: 108–1101.

Martínez-de Dios, J. R., A. Merino, F. Caballero, and A. Ollero. 2011. "Automatic Forest-Fire Measuring Using Ground Stations and Unmanned Aerial Systems." *Sensors* 11: 6328–6353.

Mermoz, M., and T. Kitzberger. 2005. "Landscape Influences on Occurrence and Spread of Wildfires in Patagonian Forests and Shrublands." *Ecology* 86: 2705–2715.

Myneni, R. B., F. Hall, P. J. Sellers, and A. L. Marshak. 1995. "The Interpretation of Spectral Vegetation Indexes." *IEEE Transactions on Geoscience and Remote Sensing* 33 (2): 481–486.

O'Brien, J. J., E. Loudermilk, B. Hornsby, A. T. Hudak, B. C. Bright, M. B. Dickinson, J. K. Hiers, C. Teske, and R. D. Ottmar. 2016. "High-Resolution Infrared Thermography for Capturing Wildland Fire Behaviour – RxCADRE 2012." *International Journal of Wildland Fire* 25: 62–75.

Ononye, A. E., A. Vodacek, and E. Saber. 2007. "Automated Extraction of Fire Line Parameters from Multispectral Infrared Images." *Remote Sensing of Environment* 108: 179–188.

Riggan, P. J., and J. W. Hoffman, 2003. "FireMapper™: A Thermal-Imaging Radiometer for Wildfire Research and Operations." *Proc. of the IEEE Aerospace Conference, paper no. 1522*..
Riggan, P. J., R. G. Tissel, R. N. Lockwood, J. A. Brass, J. Heloisa, S. Miranda, A. C. Miranda, T. Campos, and R. Higgins. 2004. "Remote Measurement of Energy and Carbon Flux from Wildfires in Brazil." *Ecological Applications* 14: 855–872.
Stow, D., P. Riggan, E. Storey, and L. Coulter. 2014. "Measuring Fire Spread Rates from Repeat Pass Airborne Thermal Infrared Imagery." *Remote Sensing Letters* 5: 803–881.
Stow, D. A., L. L. Coulter, G. R. MacDonald, and C. D. Lippitt. 2016. "Evaluation of Geometric Capture and Processing Elements in the Context of a Repeat Station Imaging Approach to Registration and Change Detection." *Photogrammetric Engineering and Remote Sensing* 82: 775–788.
Uyeda, K., D. Stow, and P. Riggan. 2015. "Tracking MODIS NDVI Time Series to Estimate Fuel Accumulation." *Remote Sensing Letters* 6: 587–596.
Valero, M. M., O. Rios, C. Mata, E. Pastor, and E. Planas. 2017. "An Integrated Approach for Tactical Monitoring and Data-Driven Spread Forecasting of Wildfires." *Fire Safety Journal* 91: 835–844.
Valero, M. M., O. Rios, E. Pastor, and E. Planas. 2018. "Automated Location of Active Fire Perimeters in Aerial Infrared Imaging Using Unsupervised Edge Detectors." *International Journal of Wildland Fire* 2018 (27): 241–256.
Van Wagner, C. E. 1977. "Conditions for the Start and Spread of Crown Fire." *Canadian Journal of Forest Research* 7: 23–34.
Viedma, O., J. Quesada, I. Torres, A. De Santes, and J. M. Moreno. 2015. "Fire Severity in a Large Fire in a *Pinus Pinaster* Forest Is Highly Predictable from Burning Conditions, Stand Structure, and Topography." *Ecosystems* 18: 237–250.